



**HAL**  
open science

# Multifiber finite element model based on enhanced concrete constitutive law to account for the effects of early age damage on the seismic response of RC structures

Chaimaa Jaafari, Stéphane Grange, David Bertrand, Jean François Georgan, Fabien Delhomme, Nicolas Tardif

## ► To cite this version:

Chaimaa Jaafari, Stéphane Grange, David Bertrand, Jean François Georgan, Fabien Delhomme, et al.. Multifiber finite element model based on enhanced concrete constitutive law to account for the effects of early age damage on the seismic response of RC structures. *Engineering Structures*, 2022, 256, pp.113987. 10.1016/j.engstruct.2022.113987 . hal-03638903

**HAL Id: hal-03638903**

**<https://hal.science/hal-03638903>**

Submitted on 12 Jul 2022

**HAL** is a multi-disciplinary open access archive for the deposit and dissemination of scientific research documents, whether they are published or not. The documents may come from teaching and research institutions in France or abroad, or from public or private research centers.

L'archive ouverte pluridisciplinaire **HAL**, est destinée au dépôt et à la diffusion de documents scientifiques de niveau recherche, publiés ou non, émanant des établissements d'enseignement et de recherche français ou étrangers, des laboratoires publics ou privés.

## Multifiber finite element model based on enhanced concrete constitutive law to account for the effects of early age damage on the seismic response of RC Structures

Chaimaa Jaafari · Stéphane Grange ·  
David Bertrand · Jean François  
Georgin · Fabien Delhomme · Nicolas  
Tardif

Received: date / Accepted: date

**Abstract** RC structures get damaged over time due to several phenomena such as shrinkage, thermal deformations, creep and corrosion. This damage starts at early age and continues during the lifetime of the structures. In order to account for the effects of early age damage on the seismic response of RC structures, a research project combining both an experimental and numerical part was conducted. In the experimental part, two types of portal frames that evolved either in endogenous conditions (by covering them using a plastic sheet to limit drying shrinkage) or in non-endogenous conditions (no imposed con-  
verging, thus similar conditions as in site constructions) during early age, were constructed and tested at the end of 28 days using static cyclic and pseudo-dynamic tests. Experimental tests performed and monitoring techniques used (ambient vibration, digital image correlation, optical fiber) showed that early age drying shrinkage can cause an increase of the seismic vulnerability of RC structures (50 % decrease of the fundamental frequency, 33 % lateral drift increase). This article presents the multifiber finite element model based on enhanced constitutive law which allows describing the early age damage due to shrinkage, creep, thermal and mechanical strains and to simulate the static and dynamic response of the portal frames. The resolution of a THC (Thermo-Hygro-Chemical) problem allows calculating shrinkage and temperature time evolutions. In the model, creep is calculated using three viscoelastic Kelvin Voigt models in series with the  $\mu$  damage law for concrete (through the resolution of an internal equilibrium at the fiber level) whereas steel is accounted for using a Menegotto model. Results obtained using the numerical model were compared to experimental ones in order to validate the proposed model.

**Keywords** Early age damage · Drying Shrinkage · Multifiber beam model with enhanced constitutive law · Reinforced Concrete · Seismic Response · THC model · Creep model · Concrete damage

## 1 Introduction

During their aging process, RC structures get deteriorated due to many factors such as shrinkage, thermal deformations, creep or carbonation, inducing a decrease in their mechanical properties and leading in some cases to major collapses.

More particularly, early age drying shrinkage takes place during the 28 first days of the lifetime of RC constructions and is due to water exchange with the surrounding environment leading to cracks. Eurocode 2 [1] (concrete design code) allows taking into account shrinkage estimation in the computation of concrete strains, which could also be accounted for in seismic design codes (such as Eurocode 8 [2]). To more precisely quantify the effect of early age drying shrinkage on the response of RC structures, many articles were published in the literature in the last decade mainly in Japan. In 2017 an article published by Maruyama [3], showed that early age drying shrinkage induces a decrease of the stiffness and natural frequency of RC structures through a FEM model. Unfortunately, in this article no experimental test was presented to validate the proposed numerical model. Nakarai [4] and Sasano [5] in 2016 and 2018 presented finite element models that allowed simulating the effect of early age drying shrinkage on the static response of RC structures. Obtained numerical results were compared to experimental ones obtained by performing monotonic and static cyclic tests. Unfortunately numerical models were not able to reproduce accurately experimental results. Mazars in 2018 [6], as part of the French CEOS program, showed using both a multifiber model and cyclic tests that the natural frequency of a RC beam subjected to early-age restrained shrinkage is highly affected. The article by Sasano in 2018 [7] showed that curing conditions influence the mechanical behavior of RC shear walls (46 % decrease of the natural frequency) using both an experimental approach and a Rigid-Body Spring Model (RBSM). Regarding the effect of drying shrinkage on the dynamic behavior of RC structures, Chijiwa in 2015 [8] [9] presented experimental and numerical results obtained on a 6 story building. Tested building was kept in non-endogenous conditions and tested using a shaking table. No similar building was tested while being kept in endogenous conditions for comparison. Furthermore, additional damage sources were significant (thermal deformations, corrosion) in the considered building. Therefore, drying shrinkage effects were not exclusively quantified.

In order to quantify and model the effects of early age drying shrinkage on the seismic response of RC structures, the GEOMAS lab of INSA Lyon conducted both an experimental and numerical research program [10]. The experimental framework that was used to underline the effects of Early Age (EA) drying shrinkage on damage evolution, static and dynamic response of two groups of RC portal frames was presented in [11]. A first group (composed of two portal frames) was kept in endogenous (E) conditions during early age. The portal frames of this first group were covered using a plastic sheet (48 hours after casting when formwork was removed) in a way to stop water exchange with the surrounding environment from occurring and thus to limit early age drying

shrinkage from happening. A second group of portal frames (composed of two portal frames) was kept in non-endogenous (NE) conditions (No imposed covering during early age after 48 hours of casting when formworks were removed). At the end of the early age period (28 days) one portal frame of each group was subjected to a static cyclic loading to determine its non-linear static response. During the static cyclic tests, the structures were instrumented using displacement (LVDT) and load sensors. The two remaining portal frames (one of each group) were followed during their (EA) period using velocimeters and optical fibers and then tested at the end of their early age period using the pseudo-dynamic technique [12] in order to compare their non-linear dynamic response under a low intensity accelerogram. During the pseudo-dynamic tests, the portal frames were instrumented using velocimeters, displacement and load sensors and monitored using 2D Digital Image Correlation [13]. The experimental protocol that was conducted allowed showing the effects of early age drying shrinkage on both the static and dynamic behavior of RC portal frames. Through static and pseudo-dynamic tests performed, it was concluded that the fundamental frequency of the structures under study was highly affected by early age damage (50 % loss). Frequency decrease induced a shift in the response spectrum curve even for a moderate intensity earthquake. The shift in the response spectrum curve induced a decrease of the spectral acceleration and in base shear as well as an increase of the lateral drift. Therefore, the linear dynamic response of the portal frames was affected by early age drying shrinkage.

The non-linear dynamic response obtained using the Pseudo-Dynamic (PsD) technique also underlined the effect of early age drying shrinkage on the seismic response of RC structures (more important drift). In fact, it was shown that the lateral drift increase between tested endogenous and non-endogenous portal frames in [11] induced by early age drying shrinkage was equal to 33% under a similar loading. Thus, the test setup (ambient vibration, digital image correlation, optical fiber) allowed concluding that early age drying shrinkage can have a significant effect on the structural response and in some cases can generate an increase of the seismic vulnerability of RC structures (increase of the seismic action due to a response spectra shift).

To help engineers account for early age damage on the static and dynamic behavior of structures, a numerical enhanced multifiber model was developed. By comparing numerical results with experimental ones emphasized in [11], the objective is to validate the numerical model by proving that it reproduces well results found experimentally.

The proposed model is based on the resolution of a Thermo-Hygro-Chemical (THC) model developed at the GEOMAS Lab of INSA Lyon [14] [15] (involving the work of Buffo Lacarrière [16], Mainguy [17] and Coussy [18]) in addition to a strong coupling of the  $\mu$  concrete damage law [19], which is a robust recently developed model that showed its efficiency in reproducing concrete dynamic behavior, combined with the use of an enhanced finite element multifiber approach. The proposed model allows to numerically follow

the early age damage evolution of a RC structure and to determine its static and dynamic behavior while accounting for its early age damage. A multifiber beam elements approach was adopted since studied portal frames are made of beam elements. In addition, using such robust and ergonomic procedure allows reducing computation time while obtaining accurate results, which could be useful for engineers in the practice.

The general methodology followed in order to solve the problem is summarized in Figure 1. The resolution process is composed of 3 main steps: a first step was conducted using COMSOL while the two following steps were performed on the ATL4S finite element code written in Matlab [20]. Step 1 consists in solving the THC problem on COMSOL to get the internal temperature and strain shrinkage fields within the cross-sections of the portal frames during early age knowing as inputs the external temperature and humidity evolutions that were measured experimentally using sensors. In step 2, the outputs of the THC model (which are shrinkage and internal temperature evolutions) were implemented as inputs of an enhanced multifiber numerical model that calculates the damage evolution of the portal frames (due to the input shrinkage and temperature evolutions, to creep calculated using three Kelvin Voigt viscoelastic models [21] [22] and to mechanical deformations calculated using the  $\mu$  damage model for concrete [19]). Step 3 consisted in performing either a pushover, a spectral analysis or a transient analysis using a classical multifiber model. It should be pointed out that the resolution of step 2 is based on a Shur complement condensation resolution procedure that takes into account strain rate effects and time dependency, which is original. In Figure 1,  $T_{ext}$  and  $hygro_{ext}$  are the external temperature and humidity measured during the early age period using sensors.  $T_{int}$  and  $\epsilon_{shrinkage}$  are the temperature and shrinkage evolutions within the cross-sections of the portal frames calculated using COMSOL.  $\sigma_{Final}$ ,  $\epsilon_{Final}$ ,  $P_{Final}$  and  $d_{Final}$  are stress, strain, internal force and displacement values of the different fibers of the model at the end of resolution step 2.

Section 2 describes the THC model that was calibrated and solved using the COMSOL software. Section 3 presents the resolution steps used in the enhanced multifiber model developed for the portal frames. Section 4 is on the description of the multifiber model of the portal frames (mesh choice, boundary conditions, calibration coefficients of the constitutive laws, *etc.*) and Section 5 shows results obtained from the numerical model (early age damage evolution, static non-linear pushover analysis, modal and linear spectral analysis as well as dynamic analysis). Results obtained using the numerical model were compared to experimental ones for validation. Conclusions and perspectives are presented in Section 6.

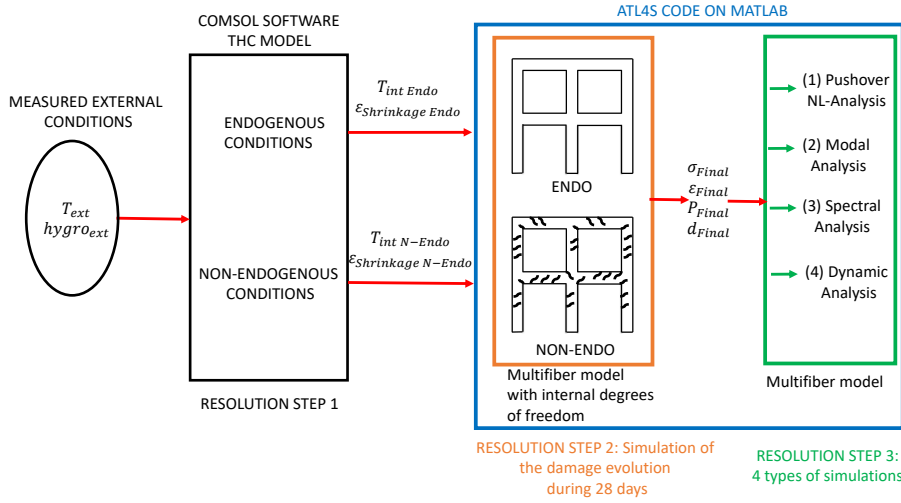


Fig. 1 Resolution steps and softwares used.

## 2 THC model (STEP 1)

### 2.1 Resolution process on COMSOL

Shrinkage due to the hydration process (Chemical Shrinkage) and due to liquid water evaporation in the environment (Drying Shrinkage) and also thermal deformations can be calculated using a THC (Thermo-hygro-chemo) model. Many models exist in the literature [16][23]. The one that was chosen to be used was developed in the GEOMAS lab [15]. It is based on the work of Buffo-Lacarrière [16], Mainguy [17] and Coussy [18]. In such model, the degree of saturation of the mortar is calculated by solving three sets of differential equations based on conservation laws [14]: liquid water, water vapour and wet air equilibrium equations. The evolution of the total porosity as well as the distribution of pores are taken into account when solving the equilibrium equations to account for early age effects. Using the equivalent pore pressure of cement based materials concept as explained by Coussy [18] shrinkage evolution is then calculated. As for thermal deformation, it is calculated by solving a heat transfer thermal conduction differential equation. All differential equations can be solved using a FEM software (COMSOL software for instance was used in this project) and model parameters have to be calibrated to account for the properties of concrete used in the structure under study. On COMSOL, the portal frames were modeled using 3D tetrahedral elements through a discretization of degree two (Lagrange quadratic discretization) and a BDF (backward differentiation formulas) integration scheme of second order was used.

## 2.2 Calibration of the THC model

The THC model was calibrated using quasi-adiabatic calorimetric tests, in addition to mass loss measurements on two groups of 4 cm by 4 cm by 16 cm prismatic specimens that have the same composition as the mortar used in the portal frames. After casting, both groups were kept during 24 hours in endogenous conditions (coverage using a plastic sheet) in a way to limit plastic shrinkage from occurring. Then, one group was kept in endogenous conditions during the remaining days of the early age period (kept covered) whereas the second group was uncovered thus allowing water exchange with the surrounding environment. Both groups were kept in the same room at a temperature of 20 °C and at a relative humidity of 50 %.

## 2.3 Inputs and outputs of the THC model

The calibrated THC model was used to determine the evolutions of shrinkage and temperature within the cross-sections of the portal frames during early age. The inputs of the THC model are the external temperature (20°C) evolution and humidity (50 %) that were measured experimentally as explained in [11].

Through interpolation, temperature and shrinkage deformation values were determined at the different concrete fibers of the multifiber model of the portal frames (Figure 2). It should be pointed out that the evolutions of temperature of the different fibers are almost similar. In fact, the portal frames have a small cross-section, thus the gradient of temperature is negligible.

Next section will explain how the multifiber beam model was enhanced in a way to take into account shrinkage and temperature evolutions calculated in COMSOL as well as in order to take into account creep and mechanical deformations. Resolution steps of such enhanced multifiber beam model will be given.

## 3 Multifiber beam model with a concrete enhanced constitutive law (STEP 2 and 3)

### 3.1 Multifiber approach

The portal frames were modeled using the multifiber beam approach ([24] [25]) as illustrated in Figure 3a. They were divided into 3D Timoshenko beam elements, where each beam element is composed of two nodes (Figure 3a). At each node there are 6 degrees of freedom: 3 rotations ( $\theta_{ix}$ ,  $\theta_{iy}$  and  $\theta_{iz}$ ) and 3 displacements ( $U_{ix}$ ,  $U_{iy}$  and  $U_{iz}$ ) and concrete fibers are located at the section Gauss points. Using shape functions, displacement values can be

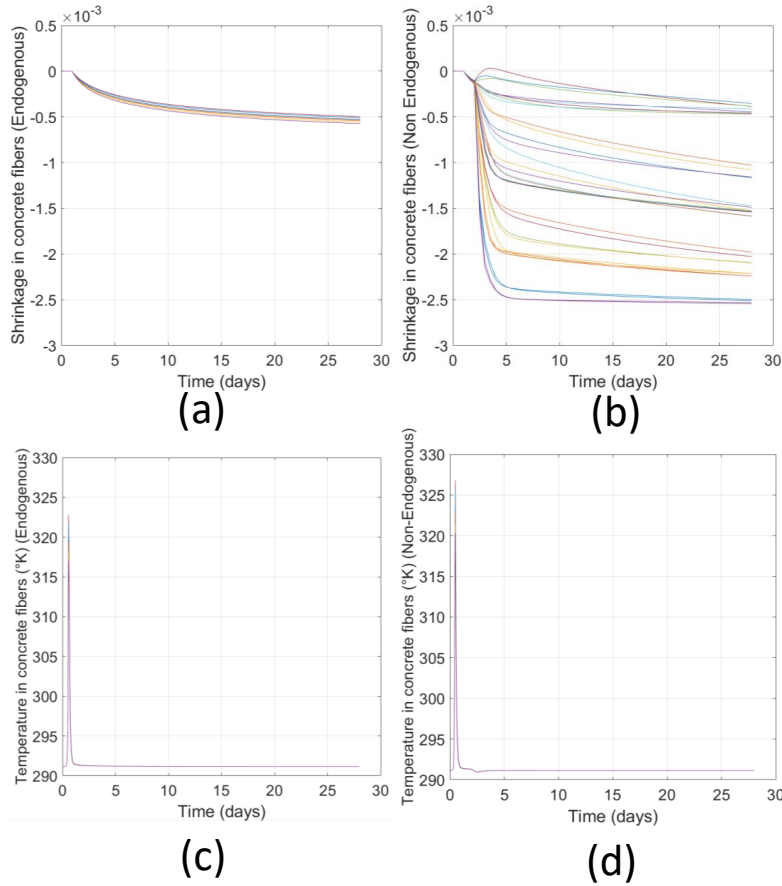


**Fig. 2** Shrinkage deformation (a) Endogenous (b) Non-Endogenous and temperature evolutions (c) Endogenous and (d) Non-Endogenous during early age (at the concrete fibers of all the elements of the portal frames: 32 fibers per element localized at the Gauss points of the concrete cross-sections.)

calculated at any point of the beam element knowing displacement values at the nodes. Timoshenko kinematic then allows determining strain values  $\epsilon$  at the different fibers knowing displacement values. Then, using a non-linear strain to stress relation stress  $\sigma$  is determined at the different fibers. Through integration over the cross section, force values  $P$  at the Gauss points of the beam elements are determined. In Figure 3a,  $\mathbf{K}$  is the stiffness matrix;  $\mathbf{a}_s$  the section compatibility matrix;  $\mathbf{B}$  the gradient metric;  $L$  the length of the beam element;  $\mathbf{U}$  the nodal displacement vector (containing nodal displacements  $U_i$  and nodal rotations  $\theta_i$ );  $\sigma$  the stress matrix;  $P$  the load vector,  $\epsilon$  the strain matrix and  $\mathbf{H}$  is the damaged Young modulus matrix.



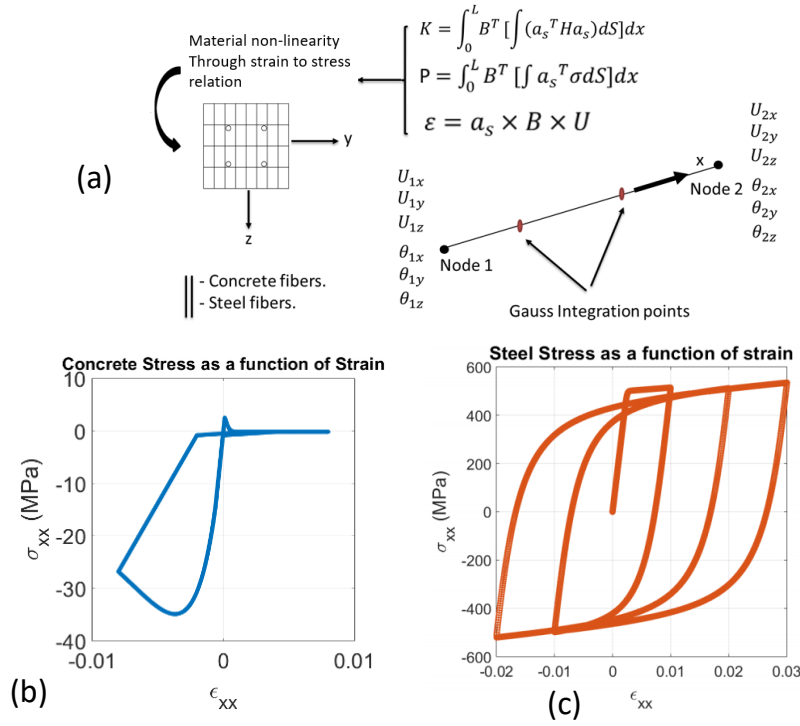


**Fig. 3** (a) Principle of the multifiber beam model ([24] [25]). Material constitutive laws: (b) concrete cyclic  $\mu$  model [19] and (c) steel cyclic model [26]

### 3.2 Concrete fibers enhanced constitutive law

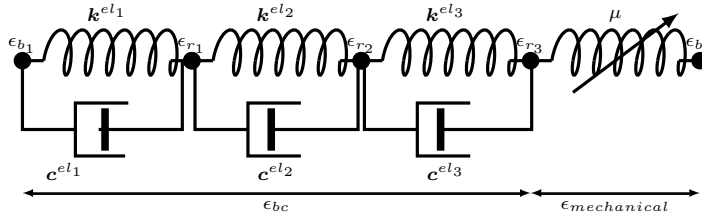


**Fig. 4** Enhanced concrete constitutive law using internal degrees of freedom.

Strains within each concrete fiber was calculated in a way to take into account the influence of shrinkage deformation  $\epsilon_{shrinkage}$ , based creep  $\epsilon_{bc}$ , thermal deformation  $\epsilon_{thermal}$ , and mechanical deformation  $\epsilon_{mechanical}$  [14]. The total deformation at a fiber element was considered to be equal to the sum of all 4 contributions.

$$\epsilon_{tot} = \epsilon_{shrinkage} + \epsilon_{thermal} + \epsilon_{bc} + \epsilon_{mechanical} \quad (1)$$

Shrinkage deformation and temperature evolutions were calculated independently using the THC model. In order to account for these values in the multifiber model, at each time step  $i$ , an internal equilibrium was solved at the concrete fiber level. The constitutive law of each concrete fiber is governed by three 1D viscoelastic elements to model creep in series with a 1D non-linear Mazars concrete  $\mu$  model (Figure 4).  $\mathbf{k}^{el_1}$ ,  $\mathbf{k}^{el_2}$ ,  $\mathbf{k}^{el_3}$ ,  $\mathbf{c}^{el_1}$ ,  $\mathbf{c}^{el_2}$  and  $\mathbf{c}^{el_3}$  are respectively the spring stiffness and damping coefficients of the viscoelastic modules (their value increases with the increase of the degree hydration [6]).  $\epsilon_{b_1}$  and  $\epsilon_{b_2}$  are the nodal external deformations and  $\epsilon_{r_1}$ ,  $\epsilon_{r_2}$  and  $\epsilon_{r_3}$  are the internal nodal deformations of the fiber constitutive law.  $\epsilon_{bc}$  is the based creep deformation while  $\epsilon_{mechanical}$  refers to the mechanical deformation (used as an input of the  $\mu$  concrete model [19]). Each rheological model returns a restoring stress and a stiffness. In order to solve the internal equilibrium, a Newton Raphson algorithm was used. Then, once the internal equilibrium of the fibers was reached, static condensation returned to the global algorithm of resolution stiffness and stress values of each fiber. Such values were then used in order to solve the global equilibrium.

Creep strain  $\epsilon_{bc}$  is the sum of strains generated by the three viscoelastic elements, whereas  $\epsilon_{mechanical}$  is the concrete mechanical uniaxial strain calculated using the  $\mu$  damage model.

The objective of the resolution process is to determine the unknown strains, derivative of strains and second derivative of strains at the internal nodes (internal degrees of freedom) ( $\epsilon_r = {}^t[\epsilon_{r_1} \ \epsilon_{r_2} \ \epsilon_{r_3}]$ ,  $\dot{\epsilon}_r = {}^t[\dot{\epsilon}_{r_1} \ \dot{\epsilon}_{r_2} \ \dot{\epsilon}_{r_3}]$ , and  $\ddot{\epsilon}_r = {}^t[\ddot{\epsilon}_{r_1} \ \ddot{\epsilon}_{r_2} \ \ddot{\epsilon}_{r_3}]$ ), knowing strain values at the external nodes (Figure 4):  $\epsilon_b = {}^t[\epsilon_{b_1} \ \epsilon_{b_2}]$ ,  $\dot{\epsilon}_b = {}^t[\dot{\epsilon}_{b_1} \ \dot{\epsilon}_{b_2}]$ , and  $\ddot{\epsilon}_b = {}^t[\ddot{\epsilon}_{b_1} \ \ddot{\epsilon}_{b_2}]$  that are provided by the global algorithm of resolution.

The strain vector of a fiber  $\mathbf{U}$  is composed of two vectors: a vector giving the strains of the external nodes  $\epsilon_b$  and a vector giving the strain of the internal nodes  $\epsilon_r$  (the derivative of strain and the second derivative of strain vectors alors also composed of external and internal contributions).

$$\mathbf{U} = \begin{bmatrix} \epsilon_b \\ \epsilon_r \end{bmatrix} \quad (2)$$

The resolution process can be divided into 5 main steps:

- Step 1: It consists in calculating the strain, derivative of strain and second derivative of strain vectors  $\epsilon_k^{el}$ ,  $\dot{\epsilon}_k^{el}$ ,  $\ddot{\epsilon}_k^{el}$  of the different internal elements knowing the nodal strains of the concrete fiber driven from the global algorithm of resolution. To achieve that, a matrix of interpolation of strains  ${}^t\mathbf{A}_b = [-1; 1]$  is used. For example the strain vector  $\epsilon_k^{el_1}$  of the first element (viscoelastic element) is calculated as follow:  $\epsilon_k^{el_1} = \epsilon_{r_1} - \epsilon_{b_1} =$

$${}^t \mathbf{A}_b {}^t [\epsilon_{b1}; \epsilon_{r1}]$$

- Step 2: Knowing the strain vector of each element, its restoring stress is calculated.
  - Since elements 1,2 and 3 are 1D viscoelastic elements, their restoring stress  $\sigma_r^{el}$  is calculated using the following expression:
 
$$\sigma_r^{el} = \mathbf{A}_b \mathbf{k}^{el} \epsilon_k^{el} + \mathbf{A}_b \mathbf{c}^{el} \dot{\epsilon}_k^{el}$$
 Where  $\mathbf{k}^{el}$ , and  $\mathbf{c}^{el}$  are respectively the spring stiffness and damping coefficients of the viscoelastic modules (their value increases with the increase of the degree hydration [6]).
  - For element 4,  $\sigma_r^{el4}$  is the stress returned by the  $\mu$  model [19] for an input strain  $\epsilon_k^{el4} = \epsilon_{b2} - \epsilon_{r3} = {}^t \mathbf{A}_b {}^t [\epsilon_{r3}; \epsilon_{r2}]$
- Step 3: The tangent operator  $\mathbf{k}_r^{el}$  of the different modules is calculated in the following way:
  - For the viscoelastic modules we have:
 
$$\mathbf{k}_r^{el} = \mathbf{A}_b \mathbf{k}^{el} {}^t \mathbf{A}_b + \mathbf{A}_b \mathbf{c}^{el} {}^t \mathbf{A}_b \frac{\gamma}{\beta \Delta t} = \mathbf{k}^{el} + \mathbf{c}^{el} \frac{\gamma}{\beta \Delta t}$$
 (matrices of size  $2 \times 2$ )
  - For element 4,  $\mathbf{k}_r^{el4}$  is the secant operator returned to the concrete  $\mu$  model law (matrix of size  $2 \times 2$ ).
- Step 4: Stresses and tangent operators of each module are then assembled in order to obtain a global restoring stress vector  $\mathbf{P}$  having 5 components and one global tangent operator matrix  $\mathbf{K}$  of size  $5 \times 5$ .  
As for the nodal strain vector of the fiber, the stress vector of the fiber  $\mathbf{P}$  and its tangent operator matrix  $\mathbf{K}$  are built from the contribution of the internal and external nodes.

$$\mathbf{P} = \begin{bmatrix} \sigma_b \\ \sigma_r \end{bmatrix} \quad \text{et} \quad \mathbf{K} = \begin{bmatrix} \mathbf{K}_{bb} & \mathbf{K}_{br} \\ \mathbf{K}_{rb} & \mathbf{K}_{rr} \end{bmatrix} \quad (3)$$

$\sigma_b$  is the stress vector (2 components) that gives stress values of the external nodes (external degrees of freedom or boundary conditions). Similarly  $\sigma_r$  is the stress vector (2 components) that gives stress values of the internal nodes.

In the tangent operator matrix  $\mathbf{K}$  terms written using index  $r$  give the contribution of the internal degrees of freedom and terms with index  $b$  provide the contribution of the external nodes (boundary conditions).

In order to determine the value of the internal degrees of freedom, a Newton Raphson loop is used. At each iteration  $i$  of the loop, the tangent operator vector  $\mathbf{K}_{rr}$  as well as a residual vector  $\mathbf{R} = -\sigma_r$  are calculated.

Once equilibrium is reached ( $\mathbf{R} = \mathbf{0}$ ):

$$\mathbf{P} = \begin{bmatrix} \sigma_b \\ -\mathbf{R} \end{bmatrix} = \begin{bmatrix} \sigma_b \\ \mathbf{0} \end{bmatrix} \quad (4)$$

At convergence, strain vector  $\mathbf{U}$  that is obtained is the one that allows reaching the equilibrium of the system. Knowing the value of vector  $\mathbf{U}$ ,

the restoring stress vector  $\mathbf{P}(\mathbf{U})$  is then calculated, in which vector component  $\sigma_b$  is the stress vector to be returned back to the global algorithm of resolution.

- Step 5: It is then possible to calculate the tangent operator of the fiber  $\tilde{\mathbf{k}}_{bb}$  (needed in the resolution of the Newton Raphson loop of the global algorithm of resolution of the structure). It links  $d\sigma_b$  to  $d\epsilon_b$ :  $d\sigma_b = \tilde{\mathbf{k}}_{bb}d\epsilon_b$ . Calculation of this tangent operator is done through static condensation of the operator  $\frac{d\mathbf{P}}{d\mathbf{U}}$  that can be expressed as:  $d\mathbf{P} = \mathbf{K}d\mathbf{U}$ , where  $\mathbf{K}$  is the tangent operator matrix assembled previously containing both the external and the internal degrees of freedom contributions.  $d\mathbf{P}$  is the increment of stress at convergence at the external degrees of freedom (nodes) whereas the increment of stress is equal to  $\mathbf{0}$  at the internal degrees of freedom at convergence.

Thus, at convergence:

$$d\mathbf{P} = \begin{bmatrix} d\sigma_b \\ -d\mathbf{R} \end{bmatrix} = \begin{bmatrix} d\sigma_b \\ \mathbf{0} \end{bmatrix} \quad (5)$$

In addition, the tangent operator  $\mathbf{K}$  and vector  $d\mathbf{P}$  satisfy the following expression:

$$\begin{bmatrix} \mathbf{K}_{bb} & \mathbf{K}_{br} \\ \mathbf{K}_{rb} & \mathbf{K}_{rr} \end{bmatrix} \begin{bmatrix} d\epsilon_b \\ d\epsilon_r \end{bmatrix} = \begin{bmatrix} d\sigma_b \\ \mathbf{0} \end{bmatrix} \quad (6)$$

Through static condensation of the internal equilibrium equation on the external equilibrium it is then possible to find the stiffness matrix to return to the global algorithm of resolution to obtain the tangent operator of the system:

$$\frac{d\sigma_b}{d\epsilon_b} = \tilde{\mathbf{k}}_{bb} = \mathbf{K}_{bb} - \mathbf{K}_{br}\mathbf{K}_{rr}^{-1}\mathbf{K}_{rb} \quad (7)$$

Thus, each concrete fiber returns its restoring stress and stiffness that are used for the determination of the sectional stiffness and sectional internal force (from which the stiffness and force of the beam elements are determined). Which allows by combining the different contributions to solve the global Newton Raphson algorithm on the global coordinate system. At each resolution step of the global Newton-Raphson loop there is a need to repeat the internal resolution steps that allow reaching the equilibrium of the fibers.

The algorithm of resolution of the internal equilibrium of a concrete fiber was summarized in Algo 3.1.

### 3.3 Steel fibers constitutive law

For steel reinforcements, a non-linear 1D Menegotto cyclic model with strain hardening [26] was used. During the early age period, the steel model was enhanced to take into account the thermal deformation of steel rebars (steel

**RESOLUTION ALGORITHM OF THE INTERNAL  
EQUILIBRIUM OF A CONCRETE FIBER AT A  
GIVEN TIME STEP  
(Newmark and Newton)**

- (i) **Extraction of the kinematic imposed to the fiber by the global algorithm of resolution**  
 $\epsilon_b = {}^t[\epsilon_{b1} \ \epsilon_{b2}]$ ,  $\dot{\epsilon}_b = {}^t[\dot{\epsilon}_{b1} \ \dot{\epsilon}_{b2}]$ , et  $\ddot{\epsilon}_b = {}^t[\ddot{\epsilon}_{b1} \ \ddot{\epsilon}_{b2}]$
- (ii) **Initialisation  $k = 1$ , extraction of the internal kinematic of the element  $\epsilon_i$ ,  $\dot{\epsilon}_i$ ,  $\ddot{\epsilon}_i$  and update (using Newmark equations):**  
 $\epsilon_r^i = {}^t[\epsilon_{r1}^i \ \epsilon_{r2}^i \ \epsilon_{r3}^i]$ ,  $\dot{\epsilon}_r^i = {}^t[\dot{\epsilon}_{r1}^i \ \dot{\epsilon}_{r2}^i \ \dot{\epsilon}_{r3}^i]$ , and  $\ddot{\epsilon}_r^i = {}^t[\ddot{\epsilon}_{r1}^i \ \ddot{\epsilon}_{r2}^i \ \ddot{\epsilon}_{r3}^i]$ ,  
(index  $i$  for initial, and  $k$  for iterations)  
 $\epsilon_r^k = \epsilon_r^i$   
 $\dot{\epsilon}_r^k = \dot{\epsilon}_r^i + (1 - \gamma)\Delta t \dot{\epsilon}_r^i + \frac{\gamma}{\beta \Delta t} [\epsilon_r^k - \epsilon_r^i - \Delta t \dot{\epsilon}_r^i - (\frac{1}{2} - \beta) \Delta t^2 \ddot{\epsilon}_r^i]$   
 $\ddot{\epsilon}_r^k = \frac{1}{\beta \Delta t^2} [\epsilon_r^k - \epsilon_r^i - \Delta t \dot{\epsilon}_r^i - (\frac{1}{2} - \beta) \Delta t^2 \ddot{\epsilon}_r^i]$
- (iii) **Evaluation of the kinematic of each element (with  ${}^tA_b = [-1 \ 1]$ ):**  
 $\epsilon_k^{el_i} = {}^tA_b {}^t[\epsilon_r^k(i-1) \ \epsilon_r^k(i)]$ ,  $\dot{\epsilon}_k^{el_i} = {}^tA_b {}^t[\dot{\epsilon}_r^k(i-1) \ \dot{\epsilon}_r^k(i)]$ ,  
 $\ddot{\epsilon}_k^{el_i} = {}^tA_b {}^t[\ddot{\epsilon}_r^k(i-1) \ \ddot{\epsilon}_r^k(i)]$
- (iv) **Calculation of the restoring stress  $\sigma_r^{el_i}$  and stiffness matrix  $\epsilon_k^{el_i}$  of each internal element:**  
 $\sigma_r^{el_i} = f(\epsilon_k^{el_i}, \dot{\epsilon}_k^{el_i}, \ddot{\epsilon}_k^{el_i})$
- (v) **Assembly of the different  $\sigma_r^{el_i}$  and  $k_r^{el}$  contributions:**  
 $\Sigma = A_{el=1}^4 \sigma_r^{el}$   
 $K = A_{el=1}^4 k_r^{el}$
- (vi) **Clear rows and columns to keep only unknown degrees of freedom (internals):**  
 $\sigma = \Sigma_r$   
 $k = K_{rr}$
- (vii) **Calculation of the residual vector  $R_k = -\sigma$ :**
- (viii) **While:  $\|R_k\| > \epsilon$**   
calculation of:  
 $(\frac{dR}{dU})_k = -k$  by assembling elementary and global matrices contributions  
 $\delta \epsilon_k = \frac{-R_k}{(\frac{dR}{d\epsilon})_k}$   
 $\epsilon_{k+1} = \epsilon_k + \delta u_k$   
 $k = k + 1$   
Re-evaluation of all the quantities at steps (ii) to (vi)  
Calculation of the residual vector of step (vii):  $R_k$
- end**
- (ix) **Extraction of the restoring stress and elementary stiffness matrix**  
 $\sigma_b = P_b$   
 $k_{bb} = K_{bb} - K_{br} K_{rr}^{-1} K_{rb}$
- (x) **END**

**Algorithm 3.1:** Algorithm of resolution of the equation of motion of a fiber having internal degrees of freedom

reinforcements are not subjected to shrinkage or creep as concrete fibers). Thus, the normal mechanical strain  $\epsilon_{xx}$  of each steel fiber was determined by subtracting to  $\epsilon_{tot}$  which is the strain contribution at the steel fiber calculated using a Timoshenko kinematic, the thermal strain as follow:

$$\epsilon_{xx} = \epsilon_{tot} - \alpha_T(T - T_0) \quad (8)$$

Where  $\alpha_T$  is the thermal expansion coefficient ( $\alpha_T = 12e^{-6}$ ),  $T$  the temperature of the steel fiber and  $T_0$  the initial temperature of the steel fiber. Knowing  $\epsilon_{xx}$ , the Menegotto law then allowed to determine the normal stress  $\sigma_{xx}$  along

the steel fiber axis. During the third step of simulations (Figure 1), the Menegotto Pinto law with strain hardening was used without taking into account the thermal deformation of the steel rebars (negligible).

#### 4 Numerical simulation of the RC frames

##### 4.1 Geometry and mesh choice

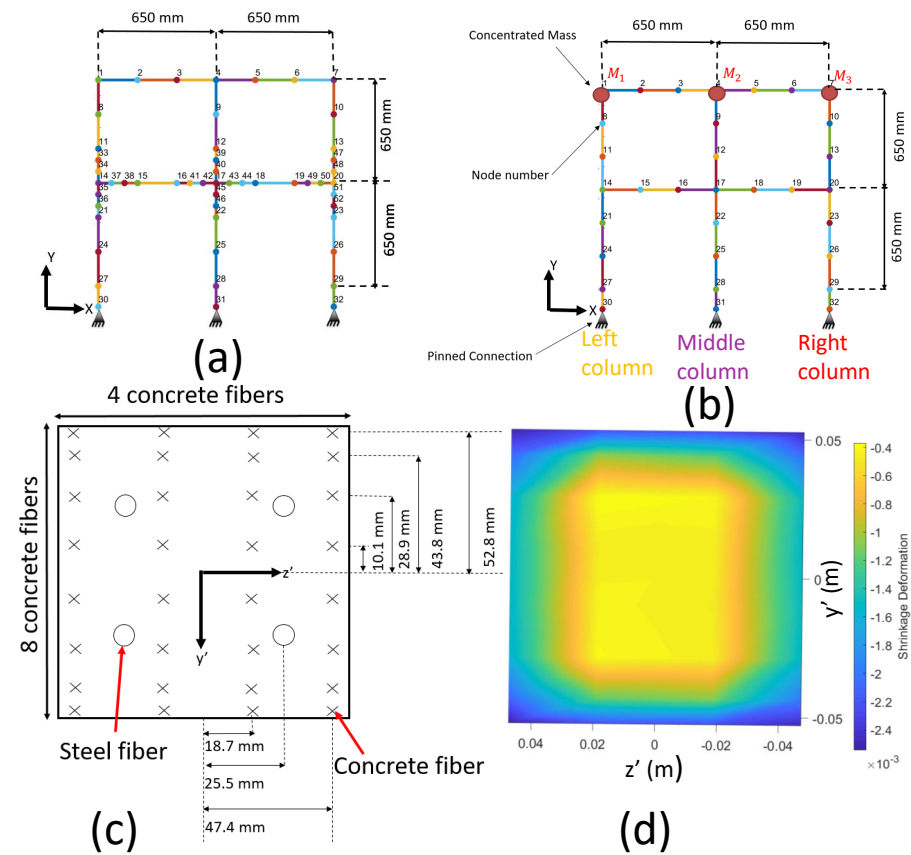


**Fig. 5** (a) Mesh used in static simulations (b) Mesh used in dynamic simulations (c) Multi-fiber cross-section (concrete fibers are localized at the Gauss points of the cross-section) and (d) Shrinkage evolution at an intermediate cross section of the portal frames interpolated at the Gauss points of a multifiber cross-section at 28 days (Non-Endogenous Case).

Figures 5a and 5b give respectively the node numbers that were used to perform static and dynamic simulations (mesh choice was made based on a

mesh sensitivity analysis).

The cross section of the portal frames was divided into 4 concrete fibers in the  $z'$  direction (to approximate the gradient of shrinkage and temperature given by COMSOL) and 8 fibers in the  $y'$  direction (parametric studies showed that 8 concrete fibers are enough to reproduce well the mechanical behavior of beam structures). In addition, 4 steel fibers were used to model longitudinal reinforcements since constructed portal frames were made of 4 longitudinal rebars (Figure 5c). Figure 5d shows the shrinkage field (non-Endogenous Portal frame) at 28 days interpolated by a multifiber cross section composed of 8 fibers in the  $y'$  direction and 4 fibers in the  $z'$  direction. It was assumed that at each time step all cross-sections of the portal frames have the same shrinkage field. It is a simplification that should be investigated in future works (through the development of an intermediate model (combining a beam model with 2D modules at the connections) using kinematic relations at the interface.

In the numerical model, 3 concentrated masses ( $M_1$ ,  $M_2$  and  $M_3$ ) (red circles) representing the contribution of upper floors were defined on top of the structures (Figures 5a and 5b).  $M_1 = M_2 = M_3 = 1148 \text{ kg}$  (simplification). Knowing that the portal frames behave as single degree of freedom systems (first mode is predominant). The total mass of the equivalent single degree of freedom is equal to  $M_{tot} = M_1 + M_2 + M_3 = 3444.4 \text{ kg}$ . Where  $M_{tot}$  is the total mass of the frame (self weight is neglected). Masses were chosen in a way to come up with realistic small scaled portal frames (1/3) (in terms of natural frequency). The same concentrated masses were simulated numerically when conducting the PsD tests [11].

#### 4.2 Enhanced boundary conditions

Structures were initially designed to be perfectly pinned at their three ends as shown in Figure 5b. During the experiment however, the portal frames underwent vertical displacements at the bottom of the three columns (as commonly observed in the practice it is very hard to achieve perfect boundary conditions). Such displacements were evaluated using digital image correlation [11]. Figure 6a shows the evolution of displacements following the vertical direction at the three ends for the endogenous and non-endogenous portal frames tested in [11]. The most important displacement occurred at the right column. Its value was implemented in the numerical model when running the non-linear dynamic analysis (Figure 7b). The two other displacements are negligible as shown experimentally (Figure 6a).

It should be pointed out that the originally measured displacement through image correlation had some inherent noise, that was filtered. Using displacement value, corresponding velocities and accelerations were then calculated (Newmark equations) for the Endogenous and Non-Endogenous portal frames. Those values were implemented in the numerical model for correction.

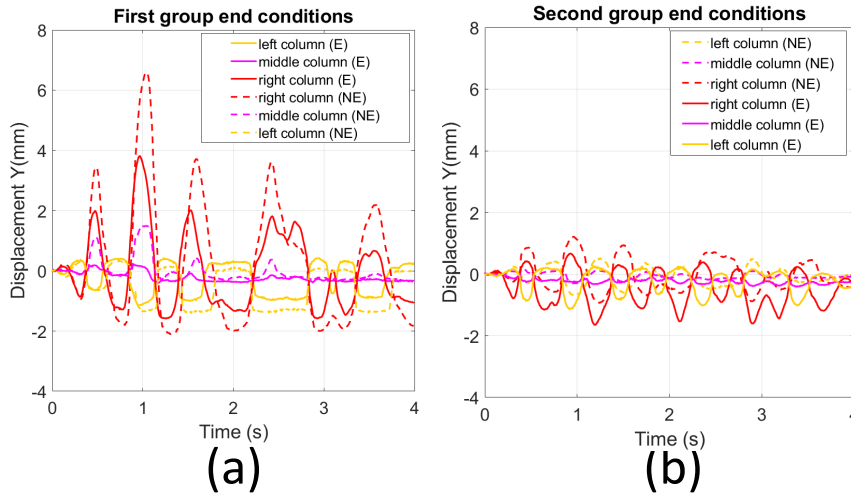


**Fig. 6** Vertical displacements (Y direction) at the bottom of the three columns of the portal frames (Figure 5b) measured using digital image correlation during PsD tests performed on two groups of portal frames (each group is composed of two portal frames) having different boundary conditions (a) Group 1 (tested in [11]) and (b) Group 2 (additional group tested using PsD tests in a way to improve boundary conditions of Group 1 [11])

Furthermore, pins were not positioned at the bottom of the portal frames as depicted in Figure 5b. Indeed, plates (including a pin) were welded to the end of the longitudinal rebars of the portal frames. After casting, the welded plates were themselves welded to a supporting beam itself fixed to the testing slab using anchors. Thus, between the pins and the bottom of the RC columns there was an eccentricity due to the plates containing the pins (Figure 7a). To account for such eccentricity in the multifiber model, 3 rigid elements having a length of 13 cm were added at the bottom of the three columns of the numerical model of the portal frames (Figure 7b). In addition, vertical displacement, velocity and acceleration determined using Digital Image correlation at the bottom of the right column were implemented into the model when conducting the dynamic analysis.

#### 4.3 Material parameters

In [11] it was explained that concrete cylindrical samples made of the same material as the portal frames have a compressive strength of 56 MPa and a tensile strength of 3 MPa, whereas their Young modulus is equal on average to 27 GPa. Due to scale effects, compressive strength, tensile strength and Young modulus values of concrete used in the portal frames are different from the ones of the cylindrical samples tested.

In order to determine material properties of concrete used in the portal frames, the  $\mu$  Mazars concrete numerical model was calibrated in a way to fit the static



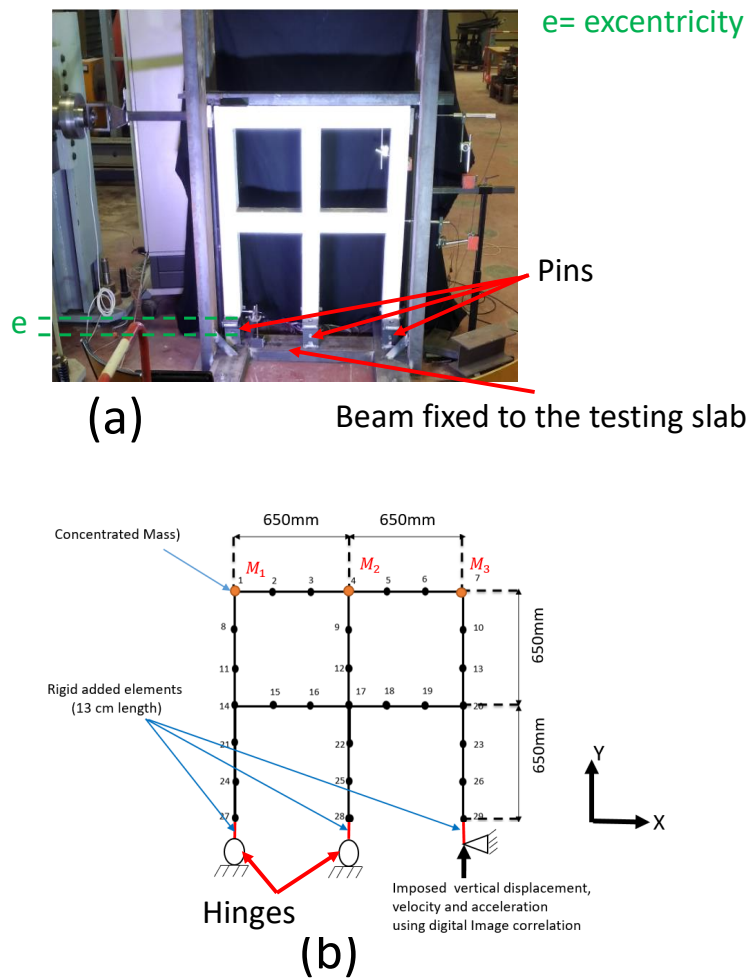


**Fig. 7** (a) Pinned connections, (b) Corrections applied to the numerical model based on experimental observations.

behavior found experimentally [11]. Concrete strength values that best approximated the static behavior of the portal frames correspond to a compressive strength of 35 MPa, a tensile strength of 2.5 MPa and a Young modulus of 24.1 GPa (value kept constant at the end of the early age period [27]). Steel reinforcements yield stress used in the numerical model was taken equal to 500 MPa. This calibration step was performed on the endogenous portal frame and the same material parameters determined for that portal frame were used when simulating the behavior of the non-endogenous portal frame. Variability of young modulus, tensile and compressive strength was also taken

into account in the multifiber model. A variability of 5% was used for Young modulus values affected to the different concrete fibers (random normal distribution with a mean value of  $E_0 = 24.1$  GPa and a standard deviation of  $E_0 \frac{5}{100}$ ).

Initial concrete parameters ( $\mu$  model [6])  $f_{t_i}$  and  $f_{c_i}$  of the different fibers were then determined starting from their respective Young modulus value  $E_i$ .  $f_{t_i} = \epsilon_{t0} \frac{E_i}{E_0}$  and  $f_{c_i} = \epsilon_{c0} \frac{E_i}{E_0}$ .  $\epsilon_{t0}$  being the mean of  $f_{t_i}$  values and  $\epsilon_{c0}$  the mean of  $f_{c_i}$  values. In our case,  $\epsilon_{c0} = -4MPa$  and  $\epsilon_{t0} = 2.5MPa$  ( $\mu$  model [6]).

Furthermore, it was observed experimentally that the longitudinal rebars were not in the reality positioned at their designed position (there was a maximum excentricity of the rebars of 27%). Such excentricity of 27% was thus imposed in the numerical model of the portal frames tested using PsD tests in [11].

#### 4.4 Constitutive laws parameters

Table 1 gives concrete and steel parameters used in the numerical model of the portal frames.

| Concrete parameters | Steel parameters | Creep parameters                                   |
|---------------------|------------------|--|
| $E = 24.1$ GPa      | $E = 210$ GPa    | $\tau_1 = 0.1$ day                                 |
| $\nu = 0.2$         | $F_y = 500$ MPa  | $\tau_2 = 1$ day                                   |
| $A_t = 0.8$         | $b = 0.0093$     | $\tau_3 = 10$ days                                 |
| $A_c = 1.2$         | $a_1 = 0$        | $k_{1\infty} = 3 \times 10^{11} \frac{\mu m}{m}$   |
| $B_t = 8000$        | $a_2 = 55$       | $k_{2\infty} = 9 \times 10^{10} \frac{\mu m}{m}$   |
| $B_c = 320$         | $a_3 = 0$        | $k_{3\infty} = 2.5 \times 10^{10} \frac{\mu m}{m}$ |
| $f_t = 2.5$ MPa     | $R_0 = 18.5$     |  |
| $f_c = -4$ MPa      | $c_{R1} = 0.925$ |  |
| $\beta_1 = 0$ MPa   | $c_{R2} = 0.15$  |  |
| $\beta_2 = 0$ MPa   |                  |  |

**Table 1** Concrete, steel reinforcements and creep model parameters.

Strain to stress relationship of concrete fibers was determined using a non-linear Mazars  $\mu$  model [19] (1.5D model). The cyclic strain to stress relation used at each concrete fiber is shown in Figure 3b, where  $\sigma_{xx}$  stands for normal stress along the concrete fiber axis and the corresponding parameters are shown in Table 1.  $E$  is the Elastic modulus,  $\nu$  the Poisson ratio,  $f_t$  is the law parameter accounting for tensile strength and  $f_c$  is the law parameter accounting for compressive strength.  $A_t$  is the first parameter governing the evolution of damage (traction),  $A_c$  is the 1<sup>st</sup> parameter governing the evolution of damage (compression) and  $B_t$  the 2<sup>nd</sup> parameter governing the evolution of damage (in traction).  $B_c$  is the 2<sup>nd</sup> parameter governing the evolution of damage in compression, while  $\beta_1$  and  $\beta_2$  are related to damping, respectively with and

without damage.  $k_{1\infty}$ ,  $k_{2\infty}$  and  $k_{3\infty}$  are the final stiffness values (at the end of the early age period) of the three viscoelastic creep modules and  $\tau_1$ ,  $\tau_2$  and  $\tau_3$  the characteristic time constants of the modules.

For steel reinforcements, a non-linear 1D Menegotto cyclic model [26] with strain hardening [28] was used as presented in Figure 3b.  $\sigma_{xx}$  stands for normal stress along the steel fiber axis. Steel law parameters are given in Table 1.  $F_y$  stands for steel yield stress, whereas  $b$ ,  $a_1$ ,  $a_2$  and  $a_3$ ,  $R_0$ ,  $C_{R1}$  and  $C_{R0}$  are calibration parameters of the Menegotto Pinto law used.

Creep was modeled using three Kelvin Voigt models in series (Figure 4). Parameters used in the creep model were determined through calibration tests [6] and are shown in Table 1.

#### 4.5 Inputs data from THC model

Shrinkage and temperature evolutions calculated using COMSOL were implemented into the multifiber model by interpolation. Figure 2 gives shrinkage and temperature evolutions used as input data of the numerical model (values at the concrete fibers). In figure 2.b, shrinkage variation between the different fibers is due to the fact that drying shrinkage is important at the outer layers of the portal frames in comparison to the internal layers.

## 5 Results

### 5.1 Early Age damage evolution

Damage evolution due to shrinkage, creep and thermal deformations of the endogenous and non-endogenous portal frames was followed during their early age period (0-28 days). Time needed to run step 2 (Figure 1) is equal to 1h13 min (with a time step of 1 hour) (Computer brand: DELL, processor: Intel(R) Core(TM) i5-8350U CPU @ 1.70GHz 1.90 GHz, RAM: 16.0 GO). Damage at the different concrete fibers remained equal to 0 in the portal frame kept in endogenous conditions as shown in Figure 8a since stress values remained below the ultimate allowable concrete tensile stress (Figure 8b). Such result is compatible with experimental observations since in the endogenous portal frame almost no cracks were observed at the end of the early age period. In the portal frame kept in non-endogenous conditions, many fibers got damaged at early age (Figure 8c) since stress reached its ultimate value  $R_t$  (Figure 8d). Concrete damage during the early age period is thus more important in the non-endogenous case than in the endogenous case because of drying shrinkage. Figure 9 shows damage maps of the different layers of the multifiber Non-Endogenous portal frame (4 layers since there are 4 fibers following the z direction) at the end of the early age period. It can be seen that damage is important at the external layers (1 and 4) of the portal frame, which is a phenomenon observed experimentally. Indeed, cracks were visible on the external

surface of the tested non-endogenous portal frames at the end of the early age period [11].

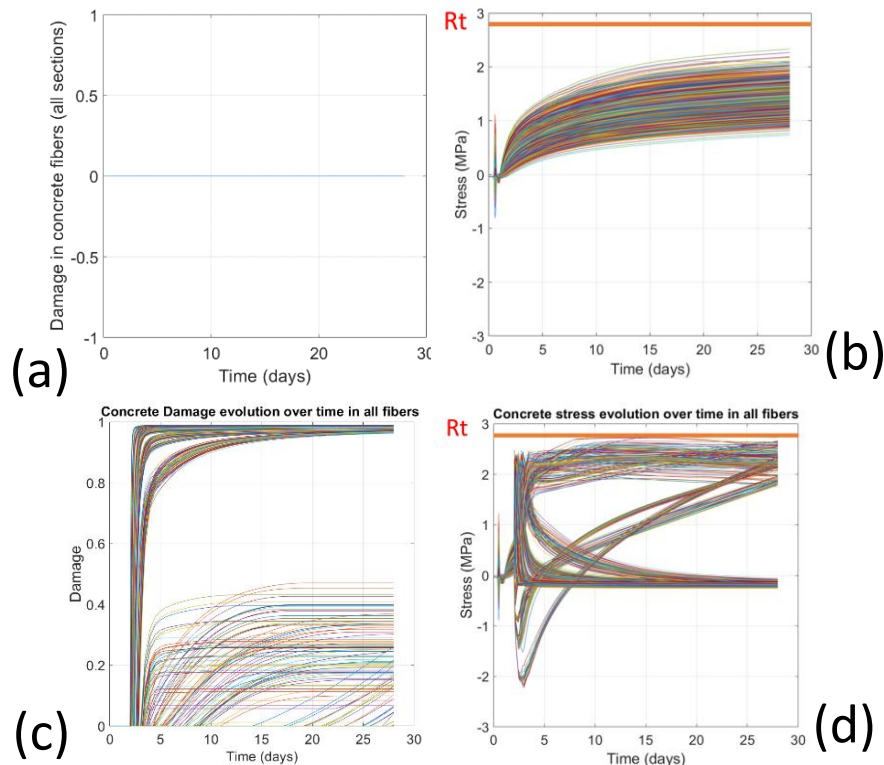


**Fig. 8** Endogenous portal frame (a) damage and (b) normal stress ( $\sigma_{xx}$ ) and Non-Endogenous portal frame (c) damage and (d) normal stress ( $\sigma_{xx}$ ) evolutions at early age in all concrete fibers (32 concrete fibers per element localized at the Gauss points of the concrete cross-sections).

## 5.2 Static Pushover

After their early age period, a pushover test was performed on the Endogenous and Non-Endogenous portal frames to compare their non-linear static response. An incremental horizontal displacement of 5 cm was imposed at node 1 (Figure 10a) until reaching the maximum capacity of the structures. Pushover curves obtained using the numerical model were plotted in Figure

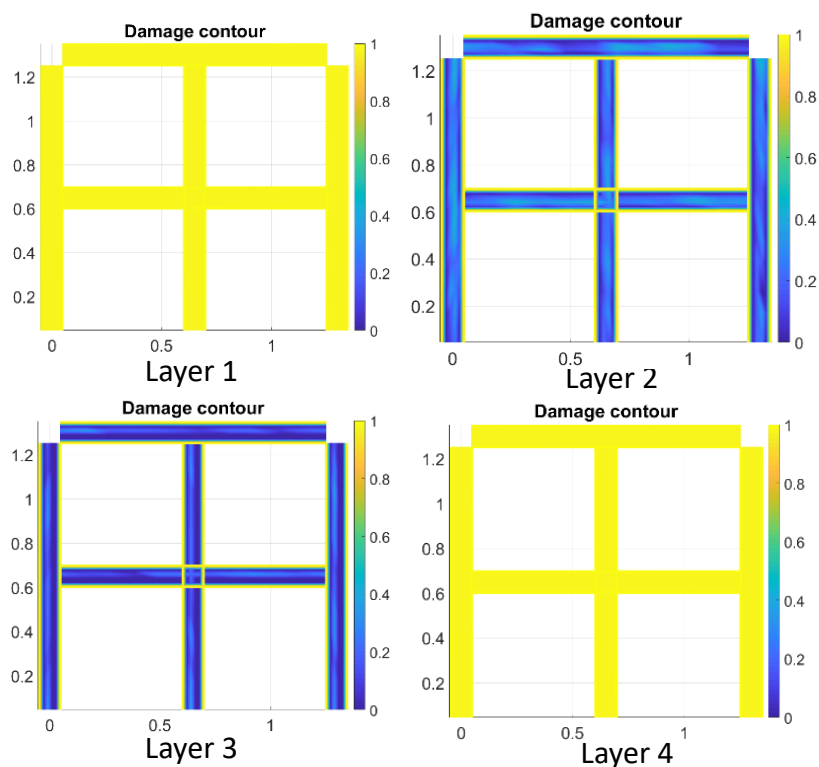


**Fig. 9** Non-Endogenous portal frame: Damage layers at the end of the early age period.

10b. It can be seen that the numerical pushover curves match well with the experimental envelope curves. The difference of initial stiffness between the endogenous portal frame and the non-endogenous portal frame captured experimentally is found numerically also. In the Endogenous case, a more important decrease of the initial stiffness is observed experimentally in comparison to numerically. It can be due to several phenomenons such as an early local damage. Numerically, a similar maximum load was obtained for the endogenous and non-endogenous portal frames, whereas experimentally a difference in maximum capacity was observed between the endogenous and non-endogenous structures. Such difference was noticed and underlined in [11]. It was observed when performing a pushover test at the end of the cyclic loading and when performing pushovers at the end of the pseudo-dynamic tests (so in total three times). Such phenomenon deserves further studies.

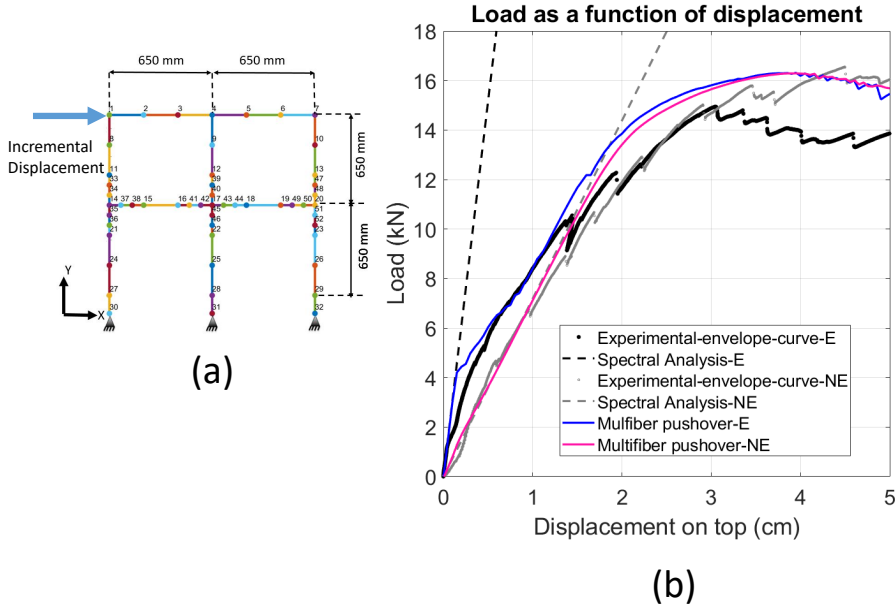


**Fig. 10** Numerical pushover analysis using the multifiber beam model: (a) Position of the imposed incremental displacement during the Pushover analysis and (b) multifiber beam model pushover results and comparison with experimental pushovers (positive envelope of cyclic test results) and spectral analysis for Endogenous (E) and Non-Endogenous (NE) portal frames

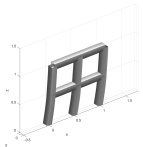
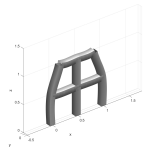
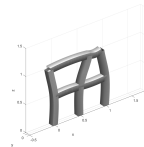
### 5.3 Modal Analysis

At the end of resolution step 2 (Figure 1) (end of the early age period), a modal analysis was performed for both groups in order to determine the natural frequencies of the portal frames as well as their mode shapes while taking into account their early age damage. The Young modulus of each fiber was multiplied by the tensile damage parameter  $D_{ti}$  (of the  $\mu$  model [19]) of the last iteration of resolution step 2.

$$E_i = E_{i0}(1 - D_{ti}) \quad (9)$$

Where  $E_i$  is the fiber young modulus to use when performing the modal analysis,  $E_{i0}$  the Young modulus of that fiber if no damage happened and  $D_{ti}$  the tensile damage scalar parameter of the fiber at the end of resolution step 2. The young modulus value  $E_i$  of each fiber allows to determine the sectional stiffness of the multifiber beam elements, from which the stiffness of each beam element is determined before calculating the stiffness of the portal frame through assembly. The 3 mode shapes of the portal frames obtained after performing modal analysis calculations are presented in Table 2. Natural frequencies were calculated after early age for both groups as shown in Table

2. Where  $f_1$  is the first natural frequency;  $f_2$  the second natural frequency and  $f_3$  the third natural frequency. The modal analysis performed showed that the first natural frequency  $f_1$  of the endogenous portal frame is 50 % higher than the natural frequency of the non-endogenous portal frame (4.8 Hz versus 2.3 Hz as shown in Table 2). Such result can be explained by the fact that in the endogenous portal frame, almost no damage happened during early age whereas an important damage occurred during the early age period in the non-endogenous portal frame due to drying shrinkage and as a consequence many concrete fibers reached their maximum allowable tensile stress.

| Mode 1  | Mode 2  | Mode 3   |
|---|---|--|
|  |  |  |
| $f_1 = 4.8 \text{ Hz (E)}$<br>$f_1 = 2.3 \text{ Hz (NE)}$                         | $f_2 = 107 \text{ Hz (E)}$<br>$f_2 = 69.5 \text{ Hz (NE)}$                        | $f_3 = 184.7 \text{ Hz (E)}$<br>$f_3 = 120 \text{ Hz (NE)}$                        |

**Table 2** Portal frame mode shapes and natural frequencies  $f_1$ ,  $f_2$  and  $f_3$  at the end of 28 days for the endogenous (E) and non-Endogenous (NE) portal frames obtained using the enhanced multifiber model.

It should be noted that the behaviour of the portal frames is mainly dictated by mode 1. Indeed, concentrated masses on top are very important compared to the self weight of the portal frames. In order to prove that, effective modal mass participation was calculated, which showed that the total mass  $M_{tot}$  of the structures is almost equal to the effective modal mass participation of mode 1. Effective modal mass participation  $m_{eff_i}$  of mode  $i$  is calculated as follows [14]:

$$m_{eff_i} = \frac{(\phi_i^T \mathbf{M} \boldsymbol{\delta})^2}{\phi_i^T \mathbf{M} \phi_i} \quad (10)$$

Where:  $\phi_i$  is the mode shape vector of mode  $i$ ;  $\mathbf{M}$  is the structure mass matrix and  $\boldsymbol{\delta}$  is the projection vector along the horizontal direction. For instance the endogenous case gives the following results:  $M_{tot} = m_{eff_1} + m_{eff_2} + m_{eff_3} \approx m_{eff_1} = 3444.4 \text{ kg}$ . Thus, the structure behaves as a one degree of freedom system of mass  $M_{tot}$ .

The first natural frequency determined using the numerical model correspond to the one found experimentally [11] (starting from stiffness values experimentally determined using cyclic tests and by considering a virtual mass

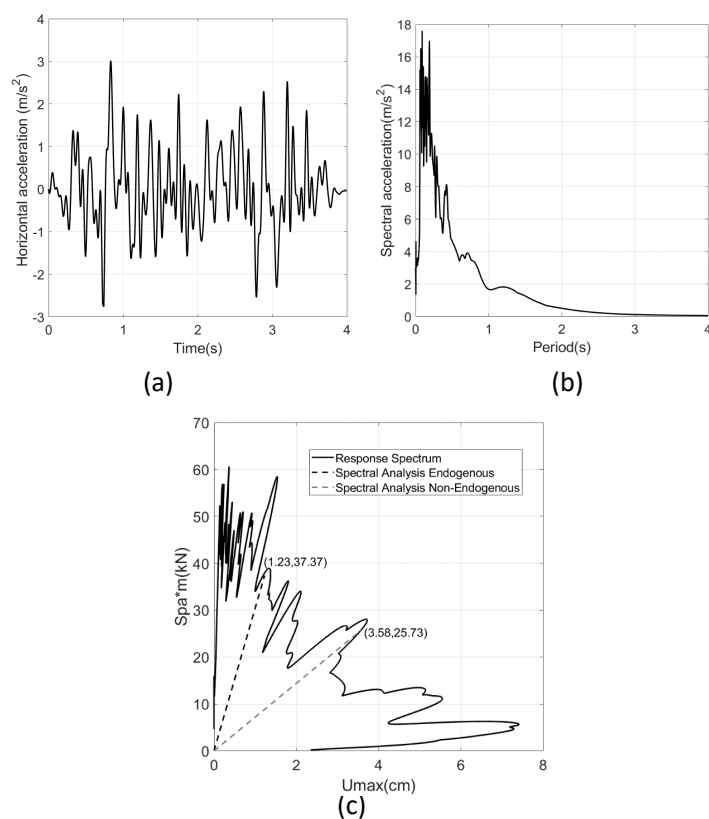


**Fig. 11** Spectral Analysis (a) 0.3 g Accelerogram, (b) Pseudo-acceleration response spectrum, (c) Spectral analysis results. Figures taken from [11]

equal to  $M_{tot}$ ). In addition, since the participation of mode 1 is highly preponderant, a similar mode shape was also obtained experimentally.

#### 5.4 Spectral Analysis

Modal analysis showed that there is a difference in behaviour between the portal frame that was kept in endogenous conditions and the one that was kept in non-endogenous conditions (change in frequency content as observed experimentally).

This difference can be further illustrated if we perform a spectral analysis on the portal frames using the same moderate intensity non-linear Time History as the one presented in [11] (Figure 11a). Its corresponding response spectrum is also given in Figure 11b. Spectral Analysis conducted on the two



types of portal frames showed (Figure 11c) that the maximum base shear in the endogenous case is equal to 37 kN while it is equal to 26 kN in the non-endogenous case (about 30% difference). Spectral Analysis curves were also plotted in Figure 10b. Maximum Base shear is calculated by summing up base shear values  $F_i^{max}$  at each mode  $i$ .

$$F_i^{max} = \frac{S_{pa}\phi_i^T \mathbf{M} \boldsymbol{\delta}}{\phi_i^T \mathbf{M} \phi_i} \quad (11)$$

Where:  $S_{pa}$  is the spectral acceleration of mode  $i$ ;  $\phi_i$  is the mode shape value at mode  $i$ ;  $\mathbf{M}$  is the structure mass Matrix and  $\boldsymbol{\delta}$  is the projection vector.

### 5.5 Dynamic analysis

The same moderate intensity 0.3 g synthetic accelerogram used in the PsD tests was applied numerically on the portal frames (Figure 11a). Time needed to run a dynamic analysis of the portal frames using the multifiber model is 41 minutes (computer brand: DELL, processor: Intel(R) Core(TM) i5-8350U CPU @ 1.70GHz 1.90 GHz, RAM: 16.0 GO).

Results are given in Figures 12. Numerical results show that there is a significant difference in the dynamic behavior of the endogenous and non-endogenous portal frames. The same observations were made experimentally.

Numerical results match very well with the ones obtained using the PsD tests.

In addition to the first series of portal frames tested using PsD tests and presented in [11] another series of portal frames was built in a way to improve boundary conditions (By minimizing the vertical displacements). Displacement as a function of time as well as force versus displacement curves obtained using the pseudo-dynamic technique for this second group of portal frames are given in Figure 13. It can be noted that the response is different from the one of the first group of portal frames. Also, the difference between the response of the endogenous portal frame and the non-endogenous portal frame is more important in this second case (The maximum displacement on top of the non-endogenous portal frame is 44 % more important than the endogenous portal frame). It implies that depending on their boundary conditions, the behavior of structures can be different and the impact of early age damage can vary. Again, using image correlation, the real displacement at the end conditions was determined. While being very small in comparison with the first group of portal frames, it is still not equal to zero and was quantified (Figure 6b). Vertical displacement at the right column given in Figure 6b were taken into account in the numerical model.

No excentricity was accounted for in the numerical model of this second group (Group 2) since rebars were better produced.

Figure 13 gives displacement and force displacement curves of the second series of portal frames (endogenous and non-endogenous cases). Again, a good

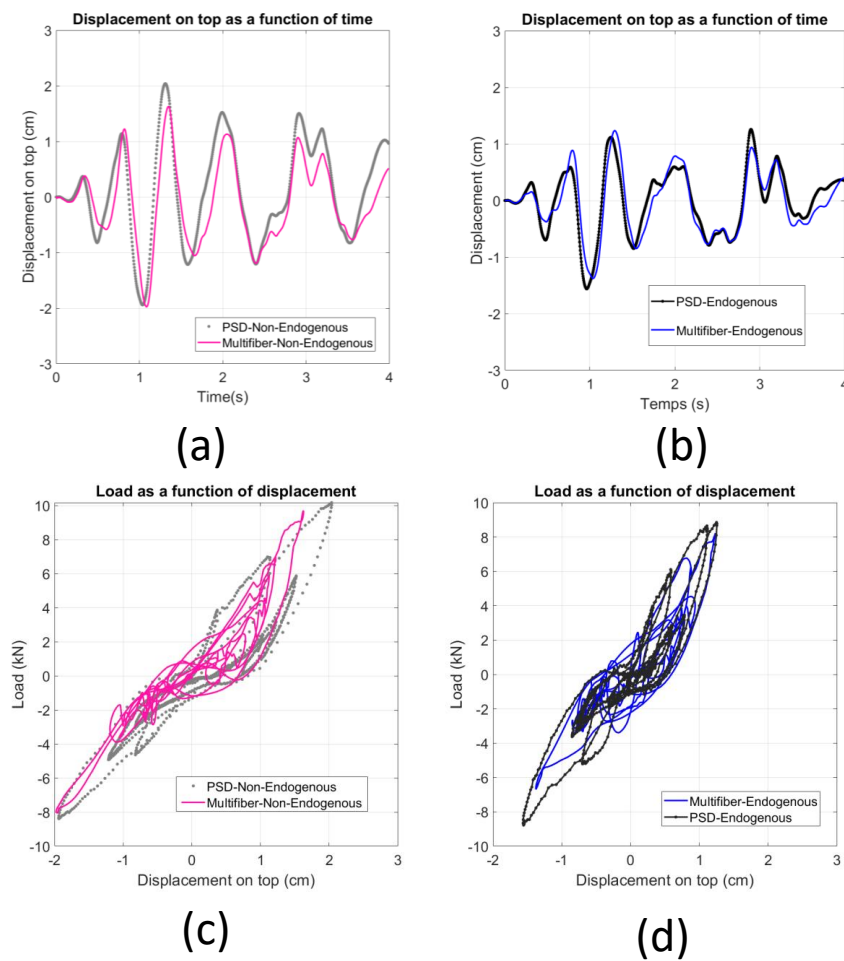


**Fig. 12** Displacements as a function of time comparison between PsD results and multifiber model in the first group (a) Non-Endogenous (b) Endogenous and Force as a function of displacement comparison between PsD results and multifiber model in the first group (c) Non-Endogenous (d) Endogenous

matching is observed between numerical simulations and experimental tests which allows validating the numerical model.

## 6 Conclusions

In this article, the numerical model developed for the portal frames was explained. First, the resolution process of the THC problem was shown. Then, a detailed explanation was given of the resolution steps involved when running a multifiber numerical model with a concrete enhanced constitutive law.

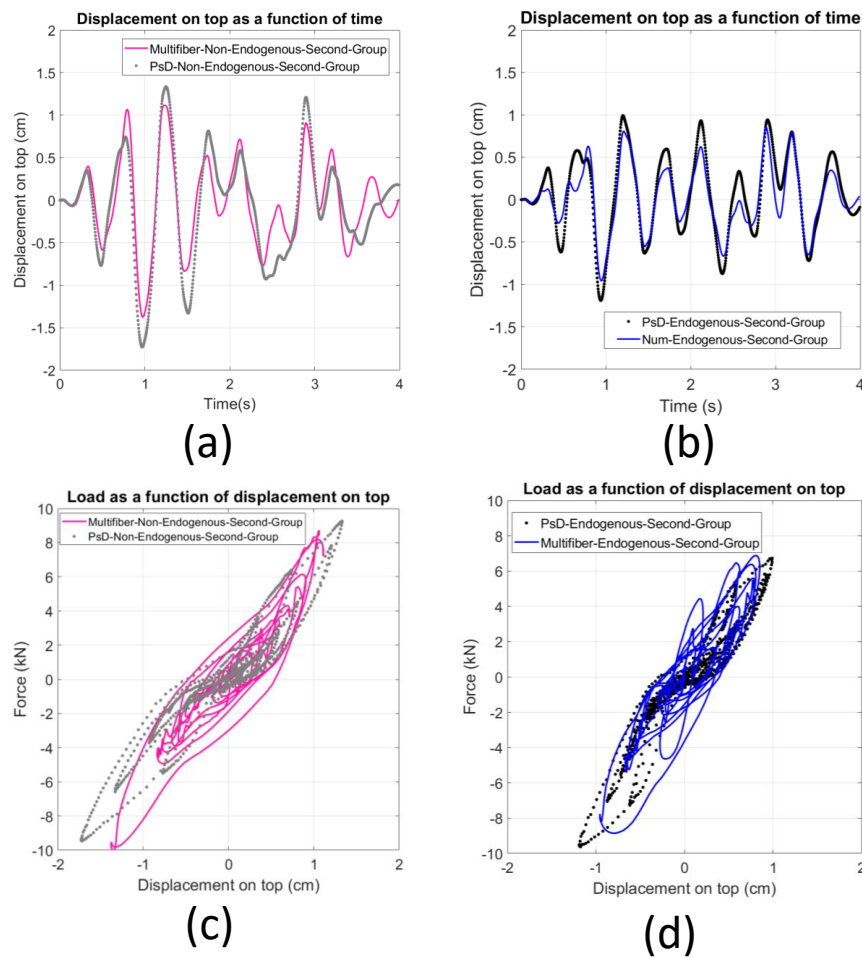


**Fig. 13** Displacements as a function of time comparison between PsD results and multifiber model in the second group (a) Non-Endogenous (b) Endogenous and Force as a function of displacement comparison between PsD results and multifiber model in the second group (c) Non-Endogenous (d) Endogenous

Such model allowed characterizing damage evolution of RC structures during early age and determining their mechanical response when subjected to static or dynamic excitations. It also accounted for experimental boundary conditions (displacement measured using Digital Image Correlation), took into account the variability of materials (Young modulus, compressive and tensile strength), as well as the excentricity of rebars observed experimentally. The model was successfully validated by comparing its results to experimental ones. Indeed, modal, spectral, pushover and dynamic analysis results obtained with the model matched very well experimental results. Numerical and experimen-

tal results showed that early age drying shrinkage causes a decrease of the natural frequency of RC structures (the natural frequency of the studied portal frames decreased by 50 % due to early age drying shrinkage). Frequency content being a design parameter, its decrease impacts the maximum base shear of the structures (30% decrease). It also impacts the seismic response of RC constructions by inducing an increase of their lateral drift (33% increase in the first tested group and 44% in the second one having different boundary conditions). Such model could be used in the future by practioners to simulate the mechanical behavior of RC structures of different dimensions and boundary conditions while accounting for early age effects. In fact, depending on the geometry of structural elements and their surface area, the influence of early age curing might be different and should be accounted for in the design process.

## Funding

This work was funded by INSA Lyon (BQR Early Quake Project).

## Conflict of interest

No potential conflict of interest was reported by the authors

## References

1. Standard, British. Eurocode 2: Design of concrete structures." Part 1-1: General rules and rules for buildings (2004): 230.
2. Standard, British. "Eurocode 8: Design of structures for earthquake resistance." Part 1 (2005): 1998-1.
3. Maruyama, Ipeei. "Multi-scale review for possible mechanisms of natural frequency change of reinforced concrete structures under an ordinary drying condition." *Journal of Advanced Concrete Technology* 14, no. 11 (2016): 691-705
4. Nakarai, Kenichiro, Shigemitsu Morito, Masaki Ehara, and Shota Matsushita. "Shear strength of reinforced concrete beams: concrete volumetric change effects." *Journal of Advanced Concrete Technology* 14, no. 5 (2016): 229-244.
5. Sasano, Hiroshi, Ipeei Maruyama, Akihiro Nakamura, Yoshihito Yamamoto, and Masaomi Teshigawara. "Impact of drying on structural performance of reinforced concrete shear walls." *Journal of Advanced Concrete Technology* 16, no. 5 (2018): 210-232
6. Mazars, Jacky, Stéphane Grange, and Matthieu Briffaut. "Simplified modeling strategy for the thermomechanical analysis of massive reinforced concrete structures at an early age." *Applied Sciences* 8, no. 3 (2018): 448.
7. Sasano, Hiroshi, Ipeei Maruyama, Akihiro Nakamura, Yoshihito Yamamoto, and Masaomi Teshigawara. "Impact of drying on structural performance of reinforced concrete shear walls." *Journal of Advanced Concrete Technology* 16, no. 5 (2018): 210-232.
8. Kurihara, Ryota, Nobuhiro Chijiwa, and Koichi Maekawa. "Thermo-hygral analysis on long-term natural frequency of RC buildings with different dimensions." *Journal of Advanced Concrete Technology* 15, no. 8 (2017): 381-396.
9. Chijiwa, Nobuhiro, and Koichi Maekawa. "Thermo-hygral case-study on full scale RC building under corrosive environment and seismic actions." *Journal of Advanced Concrete Technology* 13, no. 10 (2015): 465-478.

10. Chaimaa Jaafari. Effect of early age drying shrinkage on the seismic response of RC Structures. Civil Engineering. Université de Lyon, 2020.
11. Jaafari, Chaimaa, David Bertrand, Tina Guillot, Elodie Prudhomme, Nicolas Tardif, Jean-François Georgin, Fabien Delhomme *et al.* "Effect of early age drying shrinkage on the seismic response of RC structures." *Materials and Structures* 53, no. 6 (2020): 1-19.
12. Combescure, Didier, and Pierre Pegon. " $\alpha$ -Operator splitting time integration technique for pseudodynamic testing error propagation analysis." *Soil Dynamics and Earthquake Engineering* 16, no. 7-8 (1997): 427-443.
13. Réthoré, J. "Ufreckles." (2018).
14. Jaafari, Chaimaa, Fabien Delhomme, David Bertrand, Jean-François Georgin, and Stéphane Grange. "Impact of early age damage on the seismic response of reinforced concrete structures." *COMPADYN* 2019
15. Nguyen, Hai Trung. "Transfert hydrique dans le milieu poreux réactif: Application à l'étude de séchage d'une pâte pure ettringitique au jeune âge." PhD diss., 2018.
16. Lacarrière, Laurie. "Prévision et évaluation de la fissuration précoce des ouvrages en béton." PhD diss., Toulouse, INSA, 2007.
17. Mainguy, Marc. "Modeles de diffusion non linéaire en milieux poreux. Applications a la dissolution et au séchage des matériaux cimentaires." PhD diss., 1999.
18. Coussy, Olivier, Patrick Dangla, Thierry Lassabatère, and Véronique Baroghel-Bouny. "The equivalent pore pressure and the swelling and shrinkage of cement-based materials." *Materials and structures* 37, no. 1 (2004): 15-20.
19. Mazars, Jacky, François Hamon, and Stéphane Grange. "A new 3D damage model for concrete under monotonic, cyclic and dynamic loadings." *Materials and Structures* 48, no. 11 (2015): 3779-3793.
20. Grange, S. "ATL4S a tool and language for simplified structural solution strategy." Internal Report (2016).
21. De Schutter, Geert. "Degree of hydration based Kelvin model for the basic creep of early age concrete." *Materials and Structures* 32, no. 4 (1999): 260.
22. Briffaut, M., F. Benboudjema, Jean Michel Torrenti, and G. Nahas. "Numerical analysis of the thermal active restrained shrinkage ring test to study the early age behavior of massive concrete structures." *Engineering Structures* 33, no. 4 (2011): 1390-1401.
23. Maekawa, K., 2008. Multi-scale modeling of structural concrete. Crc Press.
24. Bitar, Ibrahim, Stéphane Grange, Panagiotis Kotronis, and Nathan Benkemoun. "A comparison of displacement-based Timoshenko multi-fiber beams finite element formulations and elasto-plastic applications." *European Journal of Environmental and Civil Engineering* 22, no. 4 (2018): 464-490.
25. P. Kotronis, J. Mazars. Simplified modelling strategies to simulate the dynamic behaviour of R/C walls. *J. Earthq. Eng* , 9, 285306, 2005.
26. Menegotto, M., and P. E. Pinto. "Method of analysis for cyclically loaded reinforced concrete plane force and bending." In *Proceedings, IABSE Symposium on Resistance and Ultimate Deformability of Structures Acted on by Well Defined Repeated Loads*, Lisbon, pp. 15-22. 1973.
27. Vu, Chi-Cong, Jérôme Weiss, Olivier Ple, David Amitrano, and Damien Vandembroucq. "Revisiting statistical size effects on compressive failure of heterogeneous materials, with a special focus on concrete." *Journal of the Mechanics and Physics of Solids* 121 (2018): 47-70.
28. Filippou, Filip C., Egor Paul Popov, and Vitelmo Victorio Bertero. "Effects of bond deterioration on hysteretic behavior of reinforced concrete joints." (1983): 137-147.